Investigating spin coupling across a three-dimensional interface in core/shell magnetic nanoparticles

C. Kons, Manh-Huong Phan, Hariharan Srikanth, D. A. Arena, Zohreh Nemati, J. A. Borchers, and K. L. Krycka

Phys. Rev. Materials **4**, 034408 — Published 23 March 2020

DOI: 10.1103/PhysRevMaterials.4.034408

Investigating spin coupling across a three-dimensional interface in core/shell magnetic nanoparticles

C. Kons, Manh-Huong Phan, Hariharan Srikanth, and D.A. Arena*

Department of Physics, University of South Florida, Tampa, Florida 33620, USA

Zohreh Nemati Porshokouh

Department of Electrical and Computer Engineering and Animal Cancer Care Research Program of the College of Veterinary Medicine, University of Minnesota, Minneapolis, MN 55455, USA

J.A. Borchers and K.L. Krycka

National Institute of Standards and Technology, Gaithersburg, Maryland 20899, USA

(Dated: 20 November 2019)

ABSTRACT

We have used a combination of x-ray magnetic circular dichroism (XMCD) spectroscopy and polarized small angle neutron scattering (P-SANS) to investigate the distribution of magnetization in heterogenous magnetic nanoparticles (NPs) consisting of a metallic Fe core / Fe-oxide shell (CS NPS) or Fe core / partial void layer / oxide shell (CVS NPs). Fe $L_{2,3}$ XMCD spectra were analyzed with a combination of experimental metallic Fe XMCD spectra and calculated L-edge spectra for the Fe cations in the oxide shell. Analyses of the temperature-dependent spectra indicate a weak variation of the relative contribution of the metallic and oxide contributions for the CS NPs, and a somewhat larger contribution from the metallic Fe core near the blocking temperature T_B of the CVS NP ensemble. The P-SANS data also indicate a larger variation in the magnetization of the CVS NPs near T_B. Modeling of the spin-dependent neutron scattering reveals large variations in the radial magnetization distribution, with a region of reversed magnetization adjacent to the metallic core. Interfacial roughness may play a role in the development of this magnetization profile.

INTRODUCTION

Magnetic nanoparticles (MNPs) have been studied extensively in recent years. The nanometer-scale of MNPs supports the emergence of magnetic properties not seen in bulk counterparts [1, 2] while the small size enables the use of MNPs for a variety of purposes. MNPs have found diverse use in fields including ferrofluids, bottoms-up synthesis of bulk ferromagnets, environmental remediation, and a wide variety of biomedical applications [3–6]. Magnetite (Fe_3O_4), and to a lesser extent maghemite (γ-Fe_2O_3), have been the most popular materials for MNPs used in biomedical and environmental applications [5, 7–10]. Both materials are variants of the spinel crystal structure with the Fe cations residing in octahedrally (O_h) or tetrahedrally (T_d) coordinated sub-lattices. Moreover, they are both *ferrimagnets* where the magnetic moments of the Fe cations are anti-aligned across the O_h and T_d sites and the net moment arises from the imbalance of the total spins on the two sublattices. The partial cancellation of atomic moments across the sublattices results in a relatively low bulk magnetization. To enhance the suitability of MNPs for various applications, bi-magnetic core-shell structures have been developed where a high-moment metallic core is used to enhance the overall magnetization and an iron oxide shell covers the core to preserve biocompatibility [5, 8].

Apart from potential biomedical and other applications, bi-magnetic core-shell nanoparticles present an interesting venue for understanding spin coupling across interfaces. Interfacial magnetic effects have become an intense area of investigation in recent years, with an emphasis on issues such as exchange bias, charge-transfer, electronic reconstructions, spin frustration, spin Seebeck effects, and Dzyaloshinskii-Moriya interactions, among others [11–15]. Generally, these effects are studied in carefully prepared thin films, where the interfaces are planar and essentially infinite (in the plane). Core / shell magnetic NPs present an alternative class of interfacial effects, where the symmetry is considerably altered (three dimensions vs. two for planar films) and also finite size effects may influence the magnetic behavior.

Spin coupling at the core/shell interface of MNPs is known to be responsible for such phenomena like exchange bias (EB), spin canting, and spin glass behavior, among others [15–18] The degree of coupling can be controlled by choice of size, structure, and composition of the core/shell constituents allowing for tunable properties [19, 20]. Control of EB

via spin coupling has been proposed as a way to combat the superparagmagnetic limit potentially leading to enhanced magnetization stability and next generation magnetic storage and recording media [16, 21, 22]. The degree of coupling along the interface can also lead to spin canting resulting in a reduced moment in the NP [23].

As in the case of planar films, the ability to tune the interactions across the three dimensional interface between the core and shell of the MNP is beneficial for both understanding the nature of the spin coupling across the interface and also for controlling the magnetic properties of the nanoparticle. We investigated changes to the interfacial spin coupling in different variants of metallic iron core / iron oxide shell nanoparticles where the core is comprised of body centered cubic α-Fe and the shell is predominantly γ-Fe_2O_3 (maghemite) [24]. We examined the interfacial spin coupling in both "pristine" α-Fe core / Fe oxide shell NPs (referred to a CS structures) and also an intermediate phase where oxygen diffusion results in a partial oxidation of the α-Fe core core leaving a void between the metal core and the oxide shell. These NP variants are termed CVS structures. The CVS structures are interesting in comparison with the CS nanoparticles as the differing contact area between the core and shell leads to a varying average coupling between the high moment / low anisotropy metallic Fe core and the ferrimagnetic / high coercivity Fe oxide shell. To examine this variable spin coupling in more detail, we utilized a combination of x-ray spectroscopy, soft x-ray absorption spectroscopy (XAS) and the related technique of x-ray magnetic circular dichroism (XMCD), as well as spin-polarized small angle neutron scattering (SANS).

In 2^{nd} row transition metals, L-edge resonant x-ray absorption processes arise via dipole-allowed optical transitions from $2p$ core level states to unoccupied $3d$ valence states. The XAS spectrum therefore provides detailed information on the chemical environment of the absorbing atom. The degree of covalency has a significant effect on the allowed transitions, where highly metallic environments produce spectra that reflect the unoccupied $3d$ density of states modulated by matrix element effects in the $2d \rightarrow 3d$ transition. Local ionic environments, on the other hand, lead to XAS profiles that are dominated by atomic-like absorption processes having both strong multiplet contributions, originating from the coupling in the final state of the $2p$ core hole and the electron excited into an available $3d$ orbital, and the additional contribution from the local ligand field [25]. For the CS and CVS MNPs the XAS and XMCD spectra will have contributions from both metallic Fe and the different Fe cations that are found in the Fe oxide shell permitting an assessment of the magnetic

contribution from the different parts of the magnetic NP.

The oxide shell in our NP variants is a partially reduced form of γ-Fe_2O_3, which has a spinel-type crystal structure with Fe^{3+} cations coordinated to nearest-neighbor oxygen cages with both octahedral (O_h) and tetrahedral (T_d) symmetry. In magnetic spinels, the dominant exchange interaction is the anti-ferromagnetic alignment of the O_h and T_d sublattices so that the net moment arises from an imbalance between the spins on the two sublattices. For the Fe based spinels γ-$Fe_2O_3$and Fe_3O_4, this leads to an XMCD spectrum with a characteristic three-peak structure for the Fe L_3 edge, where the negative peaks originate from the Fe^{3+} and Fe^{2+} cations on O_h sites and the upward peak is from the Fe^{3+} cations residing in the T_d sublattice [26]. The ratio between peak intensities can be an indicator of the relative cation population of those sites and with specific valencies.

As the absorption of an x-ray photon occurs at a single atomic site, XAS / XMCD is essentially a *local* probe of electronic and magnetic properties. Small angle neutron scattering (SANS) with a polarized neutron beam, on the other hand, provides complementary information on both average structure and magnetic correlations across a range of length scales. For ensembles of MNPs with narrow size distributions, SANS is a powerful method to examine both spin distributions within a nanoparticle as well as inter-particle spin correlations. Variation in magnitude and direction of the magnetic moment as a function of radial depth can be detected, discriminating between total reduced moments due to localized distortions versus spin canting [27].

SAMPLES AND EXPERIMENTAL METHODS

We investigated two α-Fe / γ-Fe_2O_3 variants in this study: α-Fe / γ-Fe_2O_3 core-shell structures (CS) and partially oxidized core-void-shell NPs (CVS); fully oxidized shell structures with a hollow center (H) were also studied as a reference in the XAS / XMCD measurements. The α-Fe / γ-Fe_2O_3 CS nanoparticles were synthesized via thermal decomposition of organometallic compounds. The details of the synthesis have been published elsewhere [28, 29], but briefly the synthesis involves heating of oleylamine(70%) and 1-octadecene (90%) to 140 °C under a mixture of Ar (95%) and H_2(5%) for several hours. The temperature of the solution was raised to 220 °C at which point iron pentacarbonyl, Fe $(CO_2)_5$ was injected and the solution was refluxed for 20 min. This initiated the formation of the

NPs. The reaction mixture was cooled to room temperature and the nanoparticles were then washed with ethanol and centrifuged. CVS and hollow nanoparticles were obtained by annealing at 170°C for up to 90 minutes under a flow of O_2. The final steps in the synthesis were rinsing the NPs with a 3:97 hexane:ethanol mixture, [30], separating out the MNPs with a strong permanent magnet, and drying the resulting powder of MNPs. This synthesis method is known to produce CS and CVS structures consisting of an α-Fe core surrounded by a shell of γ-Fe_2O_3 (maghemite) with an overall diameter of 15 $\pm$ 2 nm determined from transmission electron microscopy (TEM). A small portion of the powder was isolated for TEM studies of NPs size distributions and morphologies as well as magnetometry measurements.

XAS and XMCD spectra were acquired at beam line 4-ID-C at the Advanced Photon Source, Argonne National Laboratory. CS, CVS and hollow NPs were pressed into conductive carbon tape and transferred to a superconducting 7 Tesla (T) magnet equipped with a continuous flow LHe cryostat. The x-ray source for 4-ID-C is a circularly polarized undulator (CPU) and dichroism spectra were acquired by collecting pairs of scans with the CPU set to provide right or left circularly polarized (RCP or LCP) x-rays with the x-ray monochromator at the beam line configured to provide an energy resolution of 0.2 eV. Soft x-ray spectra were acquired in total electron yield mode at three different temperatures: 15 K, 95 K, and 150 K. During the cooling cycle, the samples were in a constant saturating magnetic field of $H = +5$ T oriented along the incident beam direction. XAS and XMCD scans were acquired for a constant saturating field of $\pm$ 5T for photon energies of $\sim$700 - 730 eV which spans the Fe $L_{2,3}$ core levels. At each energy point, data were collected with RCP and LCP x-rays. The average of the RCP and LCP data sets is the XAS while the difference is XMCD spectrum.

Polarized SANS measurements were recorded at the NG-7 30 m small angle scattering instrument at the NIST Center for Neutron Research [31]. We utilized a "half-polarized" experimental configuration where the incident neutron beam was polarized with FeSi super mirror before the sample environment with a fixed neutron wavelength of 0.6 nm. A calibrated precession coil ("flipper") is used to change the direction of the incident neutron beam from up spin ($\uparrow$) to down spin ($\downarrow$). The CS and CVS NPs were mounted into a recessed aluminum carrier, which was backfilled with He and sealed to prevent unwanted oxidation of the CS and CVS samples. The sample carrier was mounted on a closed cycle cryostat and

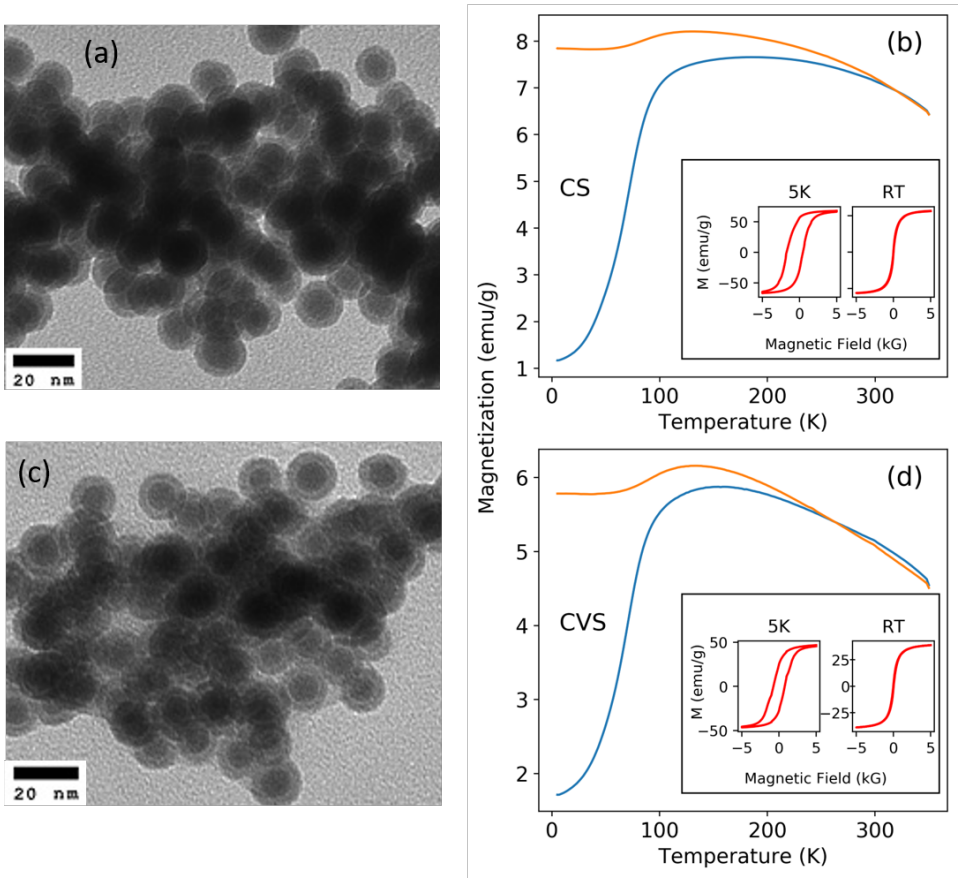

Figure 1. TEM images for the NPs used in neutron scattering study of (a) CS and (c) CVS NPs along with magnetometry in (b) and (d), respectively. The TEM images show the core / shell and core / void / shell structure. Field cooled (FC) and zero-field cooled (ZFC) M *vs*. T curves are shown. Insets to panels (b) and (d) present the field hysteresis curves at 300 K (RT) and at 5 K.

inserted into an electromagnet with a maximum field of ±1.5 T in a direction orthogonal to the neutron beam. SANS patterns were detected with a pixelated 2D detector whose distance from the sample could be varied to cover a range of scattering vectors (Q). The 2D scattering distributions were reduced using a NIST SANS data analysis package for IGOR Pro[32] and analyzed in SASView 4.2.0 [33] using a custom core/multi-shell model.

RESULTS AND ANALYSIS

Structural & Magnetic Studies

The CS shape morphology was confirmed by TEM analysis of the different NP variants, shown in Fig. 1, and size distributions were estimated from the micrographs (refer to Fig. S1 in the Supplementary Material [34]). The TEM image for the CS sample in Fig. 1-a shows a dark core / lighter shell structure while for the CVS NPs in Fig. 1-b a faint halo around around the core reveals the void layer between the core and shell. Size distributions [shown in Fig. S1] generated from these and similar TEM micrographs indicate an overall size of 15 nm ± 1-2 nm. Previous high resolution TEM studies of comparable CS NPs indicated a core diameter of ∼10 nm and an oxide shell thickness of ∼2 nm [24]. Those high resolution TEM studies also reveal the halo around the core of the CVS NPs.

Temperature dependent magnetometry ($M\,vs.\,T$) were measured under zero field cooled (ZFC) and field cooled (FC) conditions in a field of 50 Oe for all samples. Previously published blocking temperatures for the CS and CVS NPs were found to be 111K and 94K, respectively, and are consistent with the $M\,vs.\,T$ curves shown in Fig. 1 b,d [24]. Field hysteresis curves of both NPs indicate they are superparamagnetic at RT and become ferromagnetic below the blocking temperature, with coercive fields (H_c) at 5 K of 950 Oe for the CS and 750 Oe for the CVS NPs. The reduced H_c of the CVS NPs may indicate weaker exchange coupling between the soft Fe core and the high anisotropy oxide shell. Saturated magnetization (M_s) for our samples is about 70 emu / g for CS NPs and drops to around 50 emu / g for the CVS NPs. We note that there can be variations on the mass-normalized magnetization on the order of 20% between different synthesis runs. The dominant sources of the variation are the rinsing of the surfactant, small changes to the void layer in the CVS samples, and changes to the overall NP size (± 1 nm).

X-Ray Spectroscopy

Representative x-ray spectroscopy scans are presented in Fig. 2 for the CS (Fig. 2-a) and the CVS (Fig. 2-b) NPs. The XAS scans of both NP variants are remarkably similar and are indicative of nanocrystalline Fe oxide that is predominantly γ-Fe_2O_3 but also has spectral contributions from reduced Fe cations [26]. This is also consistent with reports of an

iron oxide layer that varies between Fe_3O_4 and γ-Fe_2O_3 in CS NPs [35–38]. Little spectral weight in the XAS appears to originate from the metallic Fe core. As the XAS spectra were collected via the surface-sensitive TEY mode, the dominant contribution from the surface oxide layers is reasonable. The XAS of our NPs indicates that the Fe oxide shell is slightly off the γ-Fe_2O_3 stoichiometry, with a likely spectral contribution from Fe^{2+} cations.

The XMCD spectra for both types of NPs are also presented in Fig. 2. The L_3 edge of the XMCD spectra is comprised of three main features: two prominent downward pointing peaks at 707.6 eV and 709.5 (labeled A and C in the figure) and an upward pointing peak at 708 eV (labeled B). Unlike the XAS scans, the XMCD of the NPs is quite different from both γ-Fe_2O_3 and the more reduced Fe oxide Fe_3O_4. For both γ-Fe_2O_3 and Fe_3O_4, peak B is strongly positive, with a magnitude comparable to the strongest downward pointing peak [26]. However, in our NP samples, peak B is close to the zero line for the XMCD spectrum. In the case of stoichiometric γ-Fe_2O_3, the amplitude of peak A is roughly half that of peak C, while in our case peak A is clearly larger than C.

We attribute the increased intensity of peak A to peak C to the presence of Fe^{2+} cations on O_h sites and from contributions from the metallic Fe core. We modeled the XMCD spectra of our NPs using a combination of atomic-like charge transfer multiplet calculations using the program CTM4XAS [39] for the oxide shell and an empirical α-Fe XMCD spectrum for the metallic core. We use CTM4XAS to calculate cation spectra for Fe^{2+} on O_h sites and Fe^{3+} on both O_h and T_d lattice sites. Reference XMCD spectra for the Fe cations were generated by reducing the $d-d$ and $p-d$ Slater integrals to k = 0.7 and 0.8, respectively; a crystal field of $10Dq$ = 1.2 eV was used for the $Fe^{2+,3+}_{Oh}$ cations while a value of $10Dq$ = -0.6 eV was for Fe^{3+}_{Td} cation; and an exchange field of gμBH = $\pm$ 0.01 eV for octahedral and tetrahedral sites, respectively. A Lorentzian broadening of 0.3 (0.5) eV was introduced for the L_3 (L_2) edge to account for intrinsic linewidth broadening along with an instrumental (Gaussian) broadening of 0.25 eV [25]. For the α-Fe contribution to the spectrum, we used a previously acquired XMCD spectrum from a thick Fe film deposited on a silicon substrate and capped with Al. This spectrum was also acquired in TEY mode.

All XMCD spectra were first fit assuming a linear combination of contributions from reference data for each core and shell constituents:

$$\sigma_{fit} = a\sigma_{\alpha-Fe} + b\sigma_{Fe^{2+}_{Oh}} + c\sigma_{Fe^{3+}_{Td}} + d\sigma_{Fe^{3+}_{Oh}}, \quad (1)$$

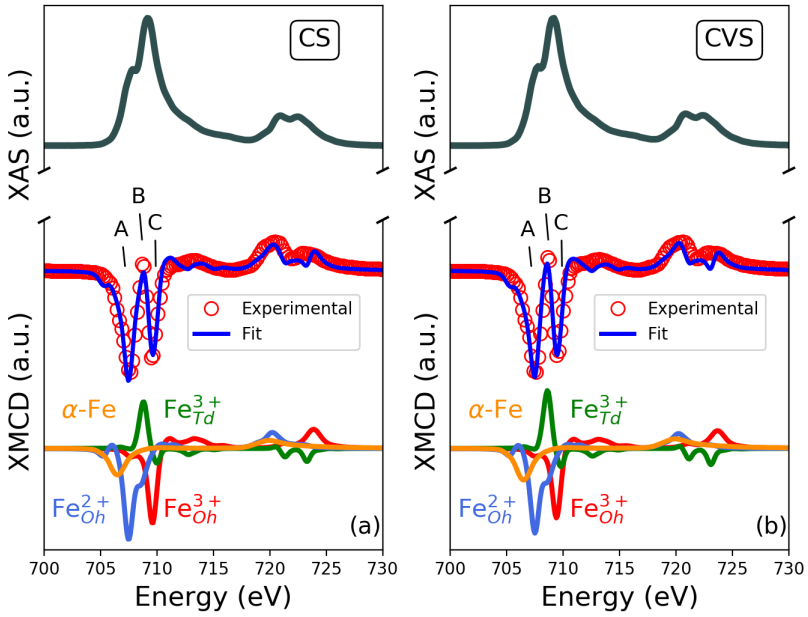

Figure 2. Experimental total electron yield (TEY) data of XAS (top) and XMCD (middle) at 95K in a 5T field with calculations of XMCD of Fe^{2+}_{Oh}, Fe^{3+}_{Td}, Fe^{3+}_{Oh} and α-Fe for (a) CS and (b) CVS NPs. The experimental spectra are shown in comparison with a normalized sum (weighted sum?) of calculated spectra (bottom).

where a, b, c, and d are fitting parameters determined by non-negative least square fitting. However, there is some energy overlap in the contributions to the XMCD spectra between α-Fe and Fe^{2+}_{Oh} that contributes to the increased intensity and broadening of peak A. This overlap tended to increase the contribution of the Fe^{2+}_{Oh} cation to the model of the spectra. To correct for this over-estimation of coefficient b, we implemented a constraint from the third NP variant, the hollow (H) NPs that do not contain a contribution from the metallic Fe core. The hollow NPs XMCD spectrum (Fig. S2 in the Supplementary Material [34]) was fit from the three calculated cation spectra resulting in a Fe^{3+}_{Oh} / Fe^{2+}_{Oh} ratio of 0.82. We assumed that the ratio of Fe cations in oxide shell of our NP variants would be stable across all measurement conditions and we used the Fe^{3+}_{Oh} / Fe^{2+}_{Oh} ratio from the hollow NPs as an additional constraint in the modeling of the the CS and CVS NPs. The Fe^{2+} cations present even in the H NPs indicate the oxide shell is slightly oxygen deficient possibly due to incomplete oxidation of the Fe at the inner interface of the H NPs.

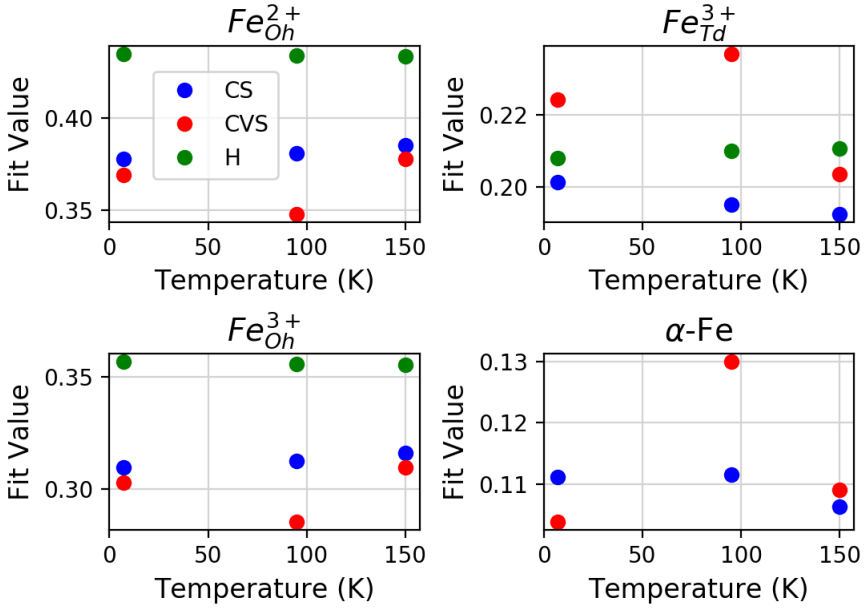

Figure 3. XMCD fitting results showing the weighted contribution of each Fe-species across all temperatures for CS, CVS, and hollow NPs.

At the bottom of Fig. 2 we present the fit to the CS and CVS XMCD spectra at 95K. As can be seen, both Fe^{3+}_{Oh} (red) and Fe^{3+}_{Td} (green) contribute to the XMCD spectra, and the relative intensity of the two anti-ferromagnetically aligned cations is comparable. The modeling also reveals a significant contribution to the spectra from Fe^{2+}_{Oh} cations (blue) indicating that the stoichiometry of the oxide shell differs from that of γ-Fe_2O_3, which should only contain Fe in a 3^+ oxidation state, to something more Fe_3O_4-like. The significant Fe^{2+}_{Oh} concentration provides an explanation for the attenuated intensity of peak B in the XMCD spectra. The Fe^{2+}_{Oh} model calculation has a strong and downward pointing shoulder at $\sim$709.3 eV which overlaps considerably with the upward peak from the Fe^{3+}_{Td} cations, partially canceling out the contribution to the XMCD spectra from the Fe cations on the T_d sub-lattice. Finally, the α-Fe core (yellow) only contributes about 10% to the overall spectral weight, but this contribution is necessary to reproduce the overall width of peak A in the XMCD spectrum. Model spectra that did not include the Fe core resulted in a very narrow spectral width for peak A that did not reproduce the data well.

We conducted similar analyses for all three NP variants (H as well as CS and CVS) at the three measurement temperatures (5 K, 95 K, and 150 K) thus examining a snapshot of the NP samples at temperatures well below, near, and well above the blocking temperature.

In Fig. 3 we summarize the results. Fit coefficient values are presented for the Fe^{2+}_{Oh}, Fe^{3+}_{Oh}, Fe^{3+}_{Td} and α-Fe for the CS and CVS NPs; the hollow NPs, which lack a core, did not contain a contribution from the α-Fe.

The coefficient values for the hollow NPs show negligible variation with temperature, indicating that the magnetic configuration of the hollow NPs does not vary with temperature under high field conditions (+5 T for the x-ray studies) [40]. To a large extent, the same holds for the CS NPs. The variation of the fit coefficients is quite small. However, in the case of the CVS NPs, there is a considerable variation in fit coefficients at 95 K. The coefficients for the O_h sites are smaller near the blocking temperature while the XMCD spectral weight from both the Fe^{3+}_{Td} cations and the α-Fe core increase.

Small Angle Neutron Scattering

As mentioned, x-ray absorption spectroscopy provides essentially *local* information on the Fe species absorbing the x-ray, and the resulting spectrum is the incoherent sum of the individual Fe atoms. In contrast, polarized neutron scattering can reveal magnetic configurations across a range of length scales. Data were collected at four temperatures ranging from 15-250 K corresponding to points above, below and near the blocking temperatures of 111 K and 94 K for the CS and CVS particle ensembles, respectively. Field cooling (FC) and zero field cooling (ZFC) were performed for each temperature with data acquired both at zero field (ZF) and high field (HF) resulting in four total field conditions; FC ZF, FC HF, ZFC ZF and ZFC HF. In the half-polarized setup, magnetic and nuclear scattering information are contained in scattering directions perpendicular to the applied field when the sample is magnetically saturated while the parallel direction contains only nuclear (non-magnetic) scattering contributions. Representative SANS profiles in the $\boldsymbol{Q} \perp \boldsymbol{H}$ direction, containing both nuclear and M$\|$ scattering contributions, are presented in Fig. 4 and Fig. 5 for the FC-HF, 75K condition. Estimated 1-σ counting errors are indicated in the graph; error estimates not presented are smaller than the marker size. The magnetic + nuclear scattering profiles in Fig. 4 show a distinct variation when the direction of the neutron spin is reversed ($I^+(\boldsymbol{Q})$ and $I^-(\boldsymbol{Q})$). In Fig. 5 we present the difference of the $I^+(\boldsymbol{Q})$ and $I^-(\boldsymbol{Q})$ scattering profiles at 75 K for the four field conditions.

The $I^+(\boldsymbol{Q})$ and $I^-(\boldsymbol{Q})$ in Fig. 4 share a number of features for both the CS (4-a) and

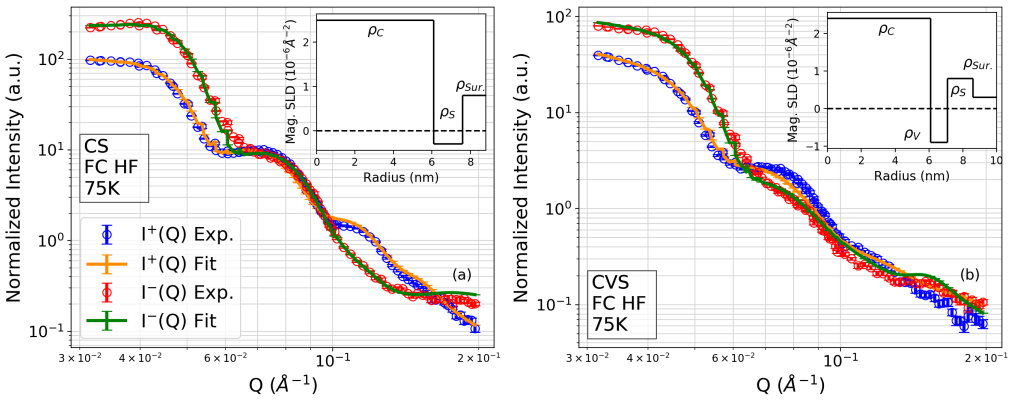

Figure 4. SANS scattering intensities perpendicular to the applied field for (a) CS and (b) CVS NPs at 75K for FC HF measurements. Data for incident neutron spins antiparallel (I^-, red) and parallel (I^+, blue) to the horizontal field were obtained by having the flipper off and on, respectively. The solids lines show the best fit for each NP using a core + multi-shell model. The inset of each plot shows the evolution of magnetic scattering length density (SLD) as a function of distance from the center of the NP.

CVS (4-b) variants. First, both data sets show structural peaks at ~0.045, 0.078 and 0.12 Q = Å^{-1}, which reflect the overall size of the NPs and their close-packed correlations. The well-resolved peaks are consistent with the narrow size distribution of the NPs seen in the TEM micrographs (Fig. 1). The data also show that the structural peaks are somewhat better defined for the CS NPs than the CVS version. Both the CS and CVS scattering profiles exhibit a "crossover" in the intensity of the $I^+(\boldsymbol{Q})$ and $I^-(\boldsymbol{Q})$ scattering between Q ~0.065 to 0.1 Å^{-1} (*cf.* slightly negative region in Fig. 5); such a "crossover" phenomenon in polarized SANS is indicative of magnetic scattering from a composite scatterer with a core / shell structure [41–43].

A structural model for each NP variant was developed by fitting $I^{\pm}(\boldsymbol{Q} \parallel \boldsymbol{H})$ as scattering parallel to the field direction contains only nuclear scattering contributions at saturating fields [27]. While TEM can provide size analysis of a local sampling region, particle dimensions determined with SANS are volume averaged throughout the entire sample and can give detailed results related to each layer of the NP [44]. The model for both NP types assumed smooth concentric layers with an outer surface layer composed of leftover surfactants or other organic materials left on the NPs after cleaning. The void layer in CVS NPs were fit

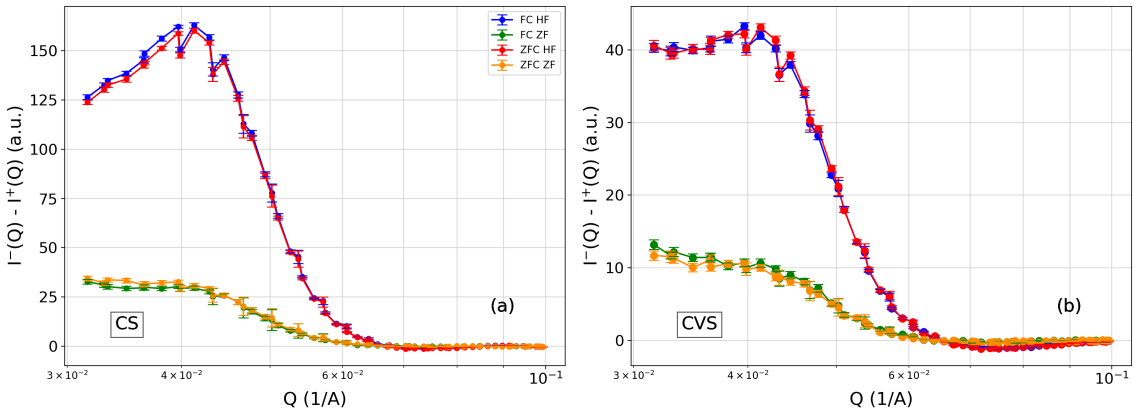

Figure 5. Magnitude of intensity difference between polarization states at 75K and various measurement field conditions for (a) CS and (b) CVS NPs.

assuming non-zero SLD values; surface roughness in the core and oxide shell layer in CVS NPs each contributed to scattering in this layer. For both NP types, the model places the core at the center of the NP while the void layer in CVS NPs could provide space for the core to shift off center. Size polydispersity was also included in the model and the metallic core produced the only significant contribution to the polydispersity. Structural parameters, including polydispersity, were determined from the SANS nuclear scattering data and were tightly constrained in the modeling of the magnetic scattering. Estimated errors in structural parameters reported below are derived from least squares fitting to the structural model.

In the CS NP the average radius for the α-Fe core was found to be 6.4 $\pm$ 0.12 nm with a polydispersity value of 7.6% while the average shell thickness for the Fe-oxide and surface layers were found to be 1.4 $\pm$ 0.06 nm and 1.2 $\pm$ 0.05 nm, respectively. In the CVS NPs the reduced core was determined to be 6.1 $\pm$ 0.17 nm in radius with a polydispersity value of 11.4% followed by a 1.0 $\pm$ 0.01 nm void, 1.7 $\pm$ 0.16 nm Fe-oxide, and 1.5 $\pm$ 0.18 nm surface layers. The thicker shell layers and, subsequently, overall diameter in the CVS NPs are consistent with other reports on this intermediate CS state when the void is formed via the Kirkendall Effect [45–47]. Since the core composition will remain the same during this process the core nuclear SLD was kept constant at $8.05{\cdot}10^{-6}$Å^{-2} corresponding to the nuclear SLD of bulk Fe while the oxide shell and surface layers were allowed to vary between NP samples when fitting. In the oxide layer this resulted in nuclear SLDs ~20% lower than

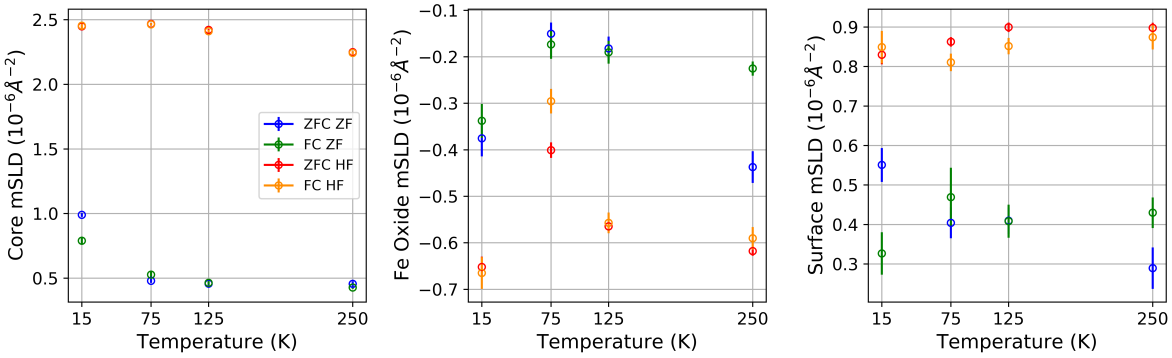

Figure 6. Temperature dependence of magnetic SLDs and field conditions in each layer in CS NPs. For the core of the NP, there is considerable overlap of the mSLDs for the ZFC HF and FC HF conditions.

tabulated values for Fe_2O_3 or Fe_3O_4 [48]. The surface layer nuclear SLD was $2.7{\cdot}10^{-6}$Å^{-2}, which is on the high side for an organic surfactant, but may also include contributions from the Fe-oxide layer originating from the surface roughness of the nanoparticle.

The insets to Fig. 4-a,b show the magnetic contributions to the SLDs (mSLD) in the FC-HF, 75 K condition calculated for the scattering models of the CS and CVS NPs; the insets show the variation of the mSLD along the radial coordinate away from the center of the NP. Note that the idealized model assumes abrupt interfaces along the radial direction. Interfacial roughness and size variations on the ensemble of NPs would tend to smooth out the radial SLD profile. Both models have a similar profile of a high moment α-Fe core with a mSLD of $\sim 2.4{\cdot}10^{-6}$Å^{-2} followed by a layer with a weakly negative mSLD and finally an outside layer with a positive mSLD. For the CS NPs, the model assumes the layer with the negative mSLD is the oxide shell, followed by the surface layer with a net positive mSLD. In contrast, for the CVS NPs the layer adjacent to the α-Fe core with the negative mSLD is modeled as the void layer, while the outer layer is divided into the oxide shell followed by the surfactant layer and both have a positive mSLD (*i.e.* the net magnetism within this layer is aligned anti-parallel to the applied magnetic field). To adequately reproduce the data across the whole Q-range presented in Fig. 4 the model requires that the layer adjacent to the metallic Fe core have a negative mSLD. Restricting the mSLD to only positive values resulted in near-zero mSLD for the shell layers and failed to capture the scattering intensity at the Q-values of the structural peaks. While the negative mSLD for

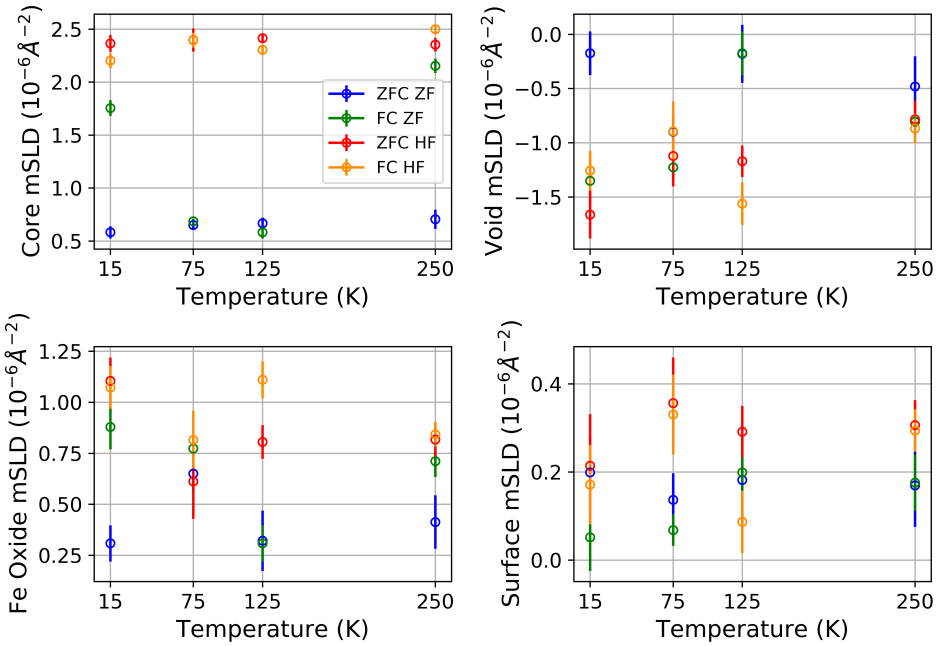

Figure 7. Temperature dependence of magnetic SLDs and field conditions in each layer in CVS NPs.

the void layer may appear to be high, we note that this contribution may come from two sources. First, for simplicity, the model assumes a concentric arrangement of core / void layer / oxide shell layer while in the actual NPs the core is likely to be off-center. Secondly, while the model allows for polydispersity of the nanoparticle dimensions in the ensemble, it assumes that the layers within a single nanoparticle have essentially zero interface roughness, with an abrupt transition from one density to the next at the radius corresponding to the transitions between the layers. The interfaces of the NPs are likely to be more complicated, with interfacial roughness as well as chemical variations along the interface.

The mSLD values for the different field conditions and temperatures are summarized in Fig. 6 for the CS NPs and Fig. 7 for the CVS variant. In CS NPs little change is seen in the core magnetic scattering across temperatures apart from a slight dip at 250K for HF measurements which mirrors the reduction in the volume magnetization at high temperature observed in the bulk magnetometry presented in Fig. 1. The zero field measurement conditions show relatively weak magnetic scattering from the core for the CS NPs, although there is an upturn in the mSLD at the lowest temperature of 15 K. The negative magnetic

SLDs in the Fe oxide shell indicate that the net spin orientation is anti-parallel to the field and the mSLD shows greater changes near the blocking temperature. Consistent with the mSLD profile presented in the inset to Fig. 4-a, the mSLD for the surface layer is aligned with the metallic Fe core, with a stronger contribution for the high-field conditions, and shows relatively little variation with temperature.

For the CVS NPs (Fig. 7), the core mSLD for both high field conditions also shows little temperature variation. The FC-ZF condition shows an unusual trend with temperature, with relatively high values at 250 K and 15 K, and weak scattering near the blocking temperature (75 K and 150 K data sets). This is clearly observed in the SANS data where the 250 K and 15 K FC-ZF conditions show a strong splitting between the $I^{+}(\boldsymbol{Q})$ and $I^{-}(\boldsymbol{Q})$ scattering cross sections and much weaker splitting at the intermediate temperatures. Similar to the CS NPs, the next layer out from the core, that is, the void layer, has a negative mSLD. However, there is a greater variation in both magnitude and temperature in the CVS NPs than in the oxide shell layer with the negative mSLD in the CS NPs. Finally, the outer parts of the CVS NPs again have a positive mSLD, but in the CVS NPs, this outermost region is modeled as two layers: oxide shell and surface layer. Generally, there is a tendency of the magnitude of the mSLD to be larger for the HF vs ZF conditions and there is also a greater variation in the mSLD near the blocking temperature.

Discussion and Conclusions

The x-ray spectroscopy and neutron scattering studies of the CS and CVS NPs reveal several interesting details about the evolution of magnetic ordering in these systems. The modeling of the the XMCD spectra allows us to track the temperature dependence of the relative contributions from the metallic core and oxide shell of the NPs. As these studies were conducted with the samples in a saturating field of +5 T, the natural expectation is that there should be little variation in the relative contribution of the different magnetic constituents of the NPs. Indeed this is what we observe in the simpler hollow NPs, where the metallic core has been fully oxidized leaving only the Fe oxide shell.

The relative contributions of the three constituent cation spectra (Fe^{3+}_{Oh}, Fe^{3+}_{Td} and Fe^{2+}_{Oh}) do not change with temperature (see green data set in Fig. 3). The contributions to the spectra of the CS NPs at saturation also do not change substantially (blue data set, Fig.

3) across the measurement temperatures. The spectral weight of the three Fe cations are all lower than the hollow NPs, as would be expected with the additional contribution from the metallic core that is lacking in the hollow NPs. However, the CVS NPs (red data set) exhibit a different behavior. While the spectral weight of the different constituents of the CVS spectra at high (150 K) and low (15 K) temperatures are generally similar to the CS values, for the 95 K data, which is close to the blocking temperature of the CVS NPs, the spectral weight of the O_h cations appears to weaken while the contributions from the Fe^{3+}_{Td} and the metallic Fe from the core increase considerably.

A similar picture of increased magnetic variation near the blocking temperature appears in the analysis of the polarized SANS data. The most striking aspect of the mSLD values for the CS NPs is the large splitting between the high-field conditions (FC-HF and ZFC-HF) and the low field measurements (FC-ZF and ZFC-ZF), which is a feature that is clearly evident for the metallic Fe core and the surface layer. The Fe oxide shell adjacent to the metallic core also generally shows a large splitting between high-field and zero-field measurements, but the difference is considerably smaller at 75 K, where the mSLD remains negative (anti-aligned with the core) but tends towards zero under all four field conditions. This may indicate that near the blocking temperature the spins of the oxide shell are becoming more disordered, leading to reduction in the magnitude of the mSLD.

The CVS NPs present a more complicated picture for the evolution of spin order with temperature. The mSLD of the metallic core for both the FC-HF and ZFC-HF conditions have values similar to the CS NPs, indicating that the core of NPs align with the applied field. Without the Zeeman energy of the applied field in the ZFC-ZF condition, the spins of the metallic Fe core randomize their directions, greatly reducing the mSLD. However the mSLD for the FC-ZF condition is anomalously high at 15 K and 250 K, that is, away from the blocking temperature of the NPs. The mSLDS at 75 K of the layers further out from the core, that is, the void and Fe oxide shell layers, have a narrow spread in values with considerable overlap of the estimated error for all four field conditions.

Overall, the pictures that emerge of the magnetic ordering of the CS and CVS NPs share some common traits. Both types of NPs have a metallic core that is strongly aligned with an external magnetic field. Moving outward from the core, the scattering indicates that the surrounding layer has a tendency to be anti-aligned with the core. In the case of the CS, this anti-aligned layer is the oxide shell while for the CVS NPs the layer is a region with a partial

overlap of the core and the oxide shell. Our modeling assumes concentric arrangement of the core, void and shell layers while in the NPs roughness along the inside surface of the oxide shell and the outer surface of the metallic Fe core will generate a non-zero mSLD and nuclear SLD for the void layer in the CVS NPs. Finally, roughness on the outer edge of the oxide shell will produce an irregular interface between the nanoparticle and the remaining surfactant on the outside, again generating non-zero SLDs but with considerably smaller values than the core. This kind of radial profile for the NPs can be seen in the insets to Fig. 4.

The SANS data are consistent with a development of the metallic core / void / oxide shell structure that does not proceed smoothly. The oxide shell that develops around the metallic Fe core is poly-crystalline, with nanocrystallites that form at energetically favorable crystal facets of the Fe core that then grow and coalesce into the oxide shell [28, 49]. The void forms preferentially via oxygen diffusion along the boundaries of the oxide nanocrystals, leading to a core that is hollowed out at irregular points along the surface of the Fe metal core [50]. A related effect is that the irregular oxygen diffusion process leads to a variation in the iron - oxygen stoichiometry. One signature of this effect is the mSLD for the surface layer of the CS NPs, which has a value for the high-field conditions that is similar to that of γ-Fe_2O_3 and Fe_3O_4 [51, 52].

The profile of the mSLD presented in the insets to Fig. 4 indicate that the desired enhancement of saturation magnetization of the metallic core / oxide shell NPs coming from the high-moment α-Fe is partially cancelled out by the adjacent layer with an anti-aligned net spin. Understanding the origin of this spin alignment would be a key step forward in developing bio-compatible, high-moment MNPs. Our experimental configuration did not allow us to examine directly the issue of spin canting at the surface of the NPs, which was shown to be an important consideration in hollow Fe-oxide NPs in our previous publication [40]. Further SANS studies using full polarization analysis would provide important additional information on the degree of spin canting and spin frustration that develops in the core/shell and core/void/shell NPs, perhaps suggesting methods to mitigate those moment-reducing interactions.

The different data sets above highlight the complementary nature of magnetic X-ray spectroscopy and neutron scattering. XMCD emphasizes the electronic states that contribute to the particle magnetism, but when conducted in TEY mode alone, XMCD can miss the

contributions of more complex spin arrangements buried inside the NPs. On the other hand, the scattering vector sensitivity of even half-polarized SANS can be inverted to produce a radial distribution of the magnetic state as presented in the insets of Fig. 4. The combination of techniques provides a more comprehensive picture of the evolution of the NP magnetization.

Acknowledgements

This research used resources of the Advanced Photon Source, a U.S. Department of Energy (DOE) Office of Science User Facility operated for the DOE Office of Science by Argonne National Laboratory under Contract No. DE-AC02-06CH11357. Access to the polarized NG7 SANS instrument was provided by the Center for High Resolution Neutron Scattering, a partnership between the National Institute of Standards and Technology and the National Science Foundation under Agreement No. DMR-1508249. We wish to thank Jeff Krzywon for his assistance with the NG7 SANS instrumentation. HS and MHP acknowledge support from the US Department of Energy, Office of Basic Energy Sciences, Division of Materials Sciences and Engineering under Award No. DE-FG02-07ER46438.

REFERENCES

* Corresponding author: darena@usf.edu

[1] T. , S. Kojima, O. Kitakami, and Y. Shimada, "Magnetic anisotropy and behaviors of fe nanoparticles," IEEE Transactions on Magnetics **37**, 2223–2225 (2001).

[2] P. Dutta, M. S. Seehra, S. Thota, and J. Kumar, "A comparative study of the magnetic properties of bulk and nanocrystalline Co_3O_4," Journal of Physics Condensed Matter **20** (2008), 10.1088/0953-8984/20/01/015218.

[3] Guandong Zhang, Yifeng Liao, and Ian Baker, "Surface engineering of core/shell iron/iron oxide nanoparticles from microemulsions for hyperthermia," Materials Science and Engineering: C **30**, 92 – 97 (2010).

[4] Jana Chomoucka, Jana Drbohlavova, Dalibor Huska, Vojtech Adam, Rene Kizek, and Jaromir Hubalek, "Magnetic nanoparticles and targeted drug delivering," Pharmacological Research **62**, 144 – 149 (2010), towards clinical applications of nanoscale medicines.

[5] Maria F. Casula, Patrizia Floris, Claudia Innocenti, Alessandro Lascialfari, Massimo Marinone, Maurizio Corti, Ralph A. Sperling, Wolfgang J. Parak, and Claudio Sangregorio, "Magnetic resonance imaging contrast agents based on iron oxide superparamagnetic ferrofluids," Chemistry of Materials **22**, 1739–1748 (2010), https://doi.org/10.1021/cm9031557.

[6] Kunal Mondal and Ashutosh Sharma, "Recent advances in the synthesis and application of photocatalytic metal–metal oxide core–shell nanoparticles for environmental remediation and their recycling process," RSC Adv. **6**, 83589–83612 (2016).

[7] Qin Zhang, Sunder S. Rajan, Katherine M. Tyner, Brendan J. Casey, Christopher K. Dugard, Yvonne Jones, Angel M. Paredes, Chekesha S. Clingman, Paul C. Howard, and Peter L. Goering, "Effects of iron oxide nanoparticles on biological responses and mr imaging properties in human mammary healthy and breast cancer epithelial cells," Journal of Biomedical Materials Research Part B: Applied Biomaterials **104**, 1032–1042 (2016), https://onlinelibrary.wiley.com/doi/pdf/10.1002/jbm.b.33450.

[8] Lenin Ramírez-Cando, "Magnetite (fe3 o4) nanoparticles: Are they really safe?" Granja-Revista de Ciencias de la Vida **21**, 76–82 (2015).

[9] W.-M. Li, S.-Y. Chen, and D.-M. Liu, "In situ doxorubicin–cap shell formation on amphiphilic gelatin–iron oxide core as a multifunctional drug delivery system with improved cytocompatibility, ph-responsive drug release and mr imaging," Acta Biomaterialia **9**, 5360 – 5368 (2013).

[10] Pradip Basnet, George K. Larsen, Ravirajsinh P. Jadeja, Yen-Con Hung, and Yiping Zhao, "α-fe2o3 nanocolumns and nanorods fabricated by electron beam evaporation for visible light photocatalytic and antimicrobial applications," ACS Applied Materials & Interfaces **5**, 2085–2095 (2013).

[11] Quy Khac Ong, Alexander Wei, and Xiao-Min Lin, "Exchange bias in Fe/fe_3o_4 core-shell magnetic nanoparticles mediated by frozen interfacial spins," Phys. Rev. B **80**, 134418 (2009).

[12] S. Banerjee, S. O. Raja, M. Sardar, N. Gayathri, B. Ghosh, and A. Dasgupta, "Iron oxide nanoparticles coated with gold: Enhanced magnetic moment due to interfacial effects," Journal of Applied Physics **109**, 123902 (2011), https://doi.org/10.1063/1.3596760.

[13] R. Ramos, T. Kikkawa, A. Anadón, I. Lucas, T. Niizeki, K. Uchida, P. A. Algarabel, L. Morellón, M. H. Aguirre, M. R. Ibarra, and E. Saitoh, "Interface-induced anomalous nernst effect in fe3o4/pt-based heterostructures," Applied Physics Letters **114**, 113902 (2019), https://doi.org/10.1063/1.5063553.

[14] K.-D. Lee, D.-J. Kim, H. Yeon Lee, S.-H. Kim, J.-H. Lee, K.-M. Lee, J.-R. Jeong, K.-S. Lee, H.-S. Song, J.-W. Sohn, S.-C. Shin, and B.-G. Park, "Thermoelectric Signal Enhancement by Reconciling the Spin Seebeck and Anomalous Nernst Effects in Ferromagnet/Non-magnet Multilayers," Scientific Reports **5**, 10249 (2015), arXiv:1504.00642 [cond-mat.mtrl-sci].

[15] D. Fiorani, L. Del Bianco, A. M. Testa, and K. N. Trohidou, "Glassy dynamics in the exchange bias properties of the iron/iron oxide nanogranular system," Phys. Rev. B **73**, 092403 (2006).

[16] D. De, Òscar Iglesias, S. Majumdar, and Saurav Giri, "Probing core and shell contributions to exchange bias in Co/co_3o_4 nanoparticles of controlled size," Phys. Rev. B **94**, 184410 (2016).

[17] Seung Ho Moon, Seung Hyun Noh, Jae-Hyun Lee, Tae Hyun Shin, Yongjun Lim, and Jinwoo Cheon, "Ultrathin interface regime of core-shell magnetic nanoparticles for effective magnetism tailoring," Nano Letters **17**, 800–804 (2017).

[18] Sayan Chandra, H. Khurshid, Wanfeng Li, G. C. Hadjipanayis, M. H. Phan, and H. Srikanth, "Spin dynamics and criteria for onset of exchange bias in superspin glass fe/γ-fe_2o_3 core-shell nanoparticles," Phys. Rev. B **86**, 014426 (2012).

[19] J. Nogués, J. Sort, V. Langlais, V. Skumryev, S. Suriñach, J.S. Muñoz, and M.D. Baró, "Exchange bias in nanostructures," Physics Reports **422**, 65 – 117 (2005).

[20] Kevin Sartori, Geoffrey Cotin, Corinne Bouillet, Valérie Halté, Sylvie Bégin-Colin, Fadi Choueikani, and Benoit P. Pichon, "Strong interfacial coupling through exchange interactions in soft/hard core–shell nanoparticles as a function of cationic distribution," Nanoscale **11**, 12946–12958 (2019).

[21] Xiaolian Sun, Natalie Frey Huls, Aruna Sigdel, and Shouheng Sun, "Tuning exchange bias in core/shell feo/fe3o4 nanoparticles," Nano Letters **12**, 246–251 (2012), pMID: 22132824, https://doi.org/10.1021/nl2034514.

[22] V. Skumryev, S. Stoyanov, Y. Zhang, G. Hadjipanayis, D. Givord, and J. Nogués, "Beating the superparamagnetic limit with exchange bias," Nature (London) **423**, 850–853 (2003).

[23] Samuel D. Oberdick, Ahmed Abdelgawad, Carlos Moya, Samaneh Mesbahi-Vasey, Demie Kepaptsoglou, Vlado K. Lazarov, Richard F. L. Evans, Daniel Meilak, Elizabeth Skoropata, Johan van Lierop, Ian Hunt-Isaak, Hillary Pan, Yumi Ijiri, Kathryn L. Krycka, Julie A. Borchers, and Sara A. Majetich, "Spin canting across core/shell fe3o4/mnxfe3-xo4 nanoparticles," Scientific Reports **8**, 3425 (2018).

[24] Z Nemati, H Khurshid, J Alonso, M H Phan, P Mukherjee, and H Srikanth, "From core/shell to hollow fe/γ-fe2o3nanoparticles: evolution of the magnetic behavior," Nanotechnology **26**, 405705 (2015).

[25] Richard A.D. Pattrick, Gerrit Van Der Laan, C. Michael B. Henderson, Pieter Kuiper, Esther Dudzik, and David J. Vaughan, "Cation site occupancy in spinel ferrites studied by x-ray magnetic circular dichroism: developing a method for mineralogists," European Journal of Mineralogy **14**, 1095–1102 (2002).

[26] E. Pellegrin, M. Hagelstein, S. Doyle, H. O. Moser, J. Fuchs, D. Vollath, S. Schuppler, M. A. James, S. S. Saxena, L. Niesen, O. Rogojanu, G. A. Sawatzky, C. Ferrero, M. Borowski, O. Tjernberg, and N. B. Brookes, "Characterization of nanocrystalline γ-fe2o3 with synchrotron radiation techniques," physica status solidi (b) **215**, 797–801 (1999).

[27] K. L. Krycka, R. A. Booth, C. R. Hogg, Y. Ijiri, J. A. Borchers, W. C. Chen, S. M. Watson, M. Laver, T. R. Gentile, L. R. Dedon, S. Harris, J. J. Rhyne, and S. A. Majetich, "Core-shell magnetic morphology of structurally uniform magnetite nanoparticles," Phys. Rev. Lett. **104**, 207203 (2010).

[28] Z. Nemati, J. Alonso, H. Khurshid, M. H. Phan, and H. Srikanth, "Core/shell iron/iron oxide nanoparticles: are they promising for magnetic hyperthermia?" RSC Adv. **6**, 38697–38702 (2016).

[29] H. Khurshid, V. Tzitzios, Wanfeng Li, C. G. Hadjipanayis, and G. C. Hadjipanayis, "Size and composition control of core-shell structured iron/iron-oxide nanoparticles," Journal of Applied Physics **107**, 09A333 (2010), https://doi.org/10.1063/1.3368720.

[30] Birju Shah, Perry T. Yin, Shraboni Ghoshal, and Ki-Bum Lee, "Multi-modal magnetic core–shell nanoparticles for effective stem-cell differentiation and imaging," Angewandte Chemie International Edition **52**, 6190–6195 (2013), https://onlinelibrary.wiley.com/doi/pdf/10.1002/anie.201302245.

[31] C. J. Glinka, J. G. Barker, B. Hammouda, S. Krueger, J. J. Moyer, and W. J. Orts, "The 30 m Small-Angle Neutron Scattering Instruments at the National Institute of Standards and Technology," Journal of Applied Crystallography **31**, 430–445 (1998).

[32] Steven R. Kline, "Reduction and analysis of SANS and USANS data using IGOR Pro," Journal of Applied Crystallography **39**, 895–900 (2006).

[33] Mathieu Doucet, Jae Hie Cho, Gervaise Alina, Jurrian Bakker, Wim Bouwman, Paul Butler, Kieran Campbell, Miguel Gonzales, Richard Heenan, Andrew Jackson, *et al.*, "Sasview version 4.2.0," Zenodo and http://www. sasview. org (2018).

[34] "See supplemental material at [url will be inserted by publisher] for additional TEM micrographs and corresponding size distributions, XAS / XMCD spectra, and SANS plots." .

[35] F. Jiménez-Villacorta, C. Prieto, Y. Huttel, N. D. Telling, and G. van der Laan, "X-ray magnetic circular dichroism study of the blocking process in nanostructured iron-iron oxide core-shell systems," Phys. Rev. B **84**, 172404 (2011).

[36] K. Fauth, E. Goering, G. Schütz, and L. Theil Kuhn, "Probing composition and interfacial interaction in oxide passivated core-shell iron nanoparticles by combining x-ray absorption and magnetic circular dichroism," Journal of Applied Physics **96**, 399–403 (2004), https://doi.org/10.1063/1.1759792.

[37] L. Theil Kuhn, A. Bojesen, L. Timmermann, K. Fauth, E. Goering, E. Johnson, M. Meedom Nielsen, and S. Mørup, "Core-shell iron–iron oxide nanoparticles: magnetic properties and interactions," Journal of Magnetism and Magnetic Materials **272-276**, 1485 – 1486 (2004), proceedings of the International Conference on Magnetism (ICM 2003).

[38] E. Skoropata, R. D. Desautels, C.-C. Chi, H. Ouyang, J. W. Freeland, and J. van Lierop, "Magnetism of iron oxide based core-shell nanoparticles from interface mixing with enhanced spin-orbit coupling," Phys. Rev. B **89**, 024410 (2014).

[39] Eli Stavitski and Frank M.F. de Groot, "The ctm4xas program for eels and xas spectral shape analysis of transition metal l edges," Micron **41**, 687 – 694 (2010).

[40] Hafsa Khurshid, Paula Lampen-Kelley, Òscar Iglesias, Javier Alonso, Manh-Huong Phan, Cheng-Jun Sun, Marie-Louise Saboungi, and Hariharan Srikanth, "Spin-glass-like freezing of inner and outer surface layers in hollow γ-fe2o3 nanoparticles," Scientific reports **5**, 15054 (2015).

[41] M. Kammel, A. Hoell, and A. Wiedenmann, "Structure of magnetite ferrofluids investigated by sans with polarized neutrons," Scripta Materialia **44**, 2341 – 2345 (2001).

[42] I. Bergenti, A. Deriu, L. Savini, E. Bonetti, and A. Hoell, "Polarised neutron investigation of iron composite nanoparticles," Journal of Applied Crystallography **36**, 450–453 (2003).

[43] A. Wiedenmann, "Small-angle neutron scattering investigations of magnetic nanostructures using polarized neutrons," Journal of Applied Crystallography **33**, 428–432 (2000), cited By 76.

[44] Cousin, Fabrice, "Small angle neutron scattering," EPJ Web of Conferences **104**, 01004 (2015).

[45] Quy Khac Ong, Xiao-Min Lin, and Alexander Wei, "Role of frozen spins in the exchange anisotropy of core-shell fe@fe3o4 nanoparticles," The Journal of Physical Chemistry C **115**, 2665–2672 (2011), pMID: 21321674.

[46] Manh-Huong Phan, Javier Alonso, Hafsa Khurshid, Paula Lampen-Kelley, Sayan Chandra, Kristen Stojak Repa, Zohreh Nemati, Raja Das, Óscar Iglesias, and Hariharan Srikanth, "Exchange bias effects in iron oxide-based nanoparticle systems," Nanomaterials **6** (2016), 10.3390/nano6110221.

[47] Hong Jin Fan, Ulrich Gösele, and Margit Zacharias, "Formation of nanotubes and hollow nanoparticles based on kirkendall and diffusion processes: A review," Small **3**, 1660–1671 (2007), https://onlinelibrary.wiley.com/doi/pdf/10.1002/smll.200700382.

[48] Zhendong Fu, Yinguo Xiao, Artem Feoktystov, Vitaliy Pipich, Marie-Sousai Appavou, Yixi Su, Erxi Feng, Wentao Jin, and Thomas Brückel, "Field-induced self-assembly of iron oxide nanoparticles investigated using small-angle neutron scattering," Nanoscale **8**, 18541–18550 (2016).

608 [49] Maria Ibáñez, Jiandong Fan, Wenhua Li, Doris Cadavid, Raquel Nafria, Alex Carrete, and
609 Andreu Cabot, "Means and limits of control of the shell parameters in hollow nanoparticles
610 obtained by the kirkendall effect," Chemistry of Materials **23**, 3095–3104 (2011).
611 [50] Abdel-Aziz El Mel, Ryusuke Nakamura, and Carla Bittencourt, "The kirkendall effect and
612 nanoscience: hollow nanospheres and nanotubes," Beilstein Journal of Nanotechnology **6**,
613 1348–1361 (2015).
614 [51] Mikhail V. Avdeev, Emmanuelle Dubois, Guillaume Mériguet, Elie Wandersman, Vasil M.
615 Garamus, Artem V. Feoktystov, and Regine Perzynski, "Small-angle neutron scatter-
616 ing analysis of a water-based magnetic fluid with charge stabilization: contrast varia-
617 tion and scattering of polarized neutrons," Journal of Applied Crystallography **42** (2009),
618 10.1107/S0021889809036826.
619 [52] Yimei Zhu, ed., "Application of polarized neutron reflectometry to studies of artificially
620 structured magnetic materials," in *Modern Techniques for Characterizing Magnetic Materials*
621 (Springer US, Boston, MA, 2005) pp. 107–155.